Journal of Materials Chemistry C

ROYAL SOCIETY OF CHEMISTRY

PAPER

View Article Online
View Journal | View Issue

Cite this: J. Mater. Chem. C, 2020, 8, 16923

Multiphoton absorption in low-dimensional cesium copper iodide single crystals†

Zhihang Guo,‡[abc] Junzi Li,‡[ad] Yang Gao,[a] Jiaji Cheng,[ac] Wenjing Zhang,[d] Ruikun Pan,*[c] Rui Chen*[b] and Tingchao He*[a]

Received 26th August 2020,
Accepted 20th October 2020

DOI: 10.1039/d0tc04061d

rsc.li/materials-c

Low-dimensional lead-free metal halides, which feature strong quantum confinement effects, have recently attracted great attention due to their excellent optical properties and favorable stability under ambient conditions. Although controllable synthetic strategies, structural characterization and linear optical properties of lead-free metal halides have been widely reported, relevant studies on their nonlinear optical properties are still lacking, which hinders their applications in nonlinear photonic devices. Herein, two types of millimeter-level high-crystallinity cesium copper halide single crystals (SCs), *i.e.*, $Cs_3Cu_2I_5$ and $CsCu_2I_3$, with high photoluminescence (PL) quantum yields, are synthesized using an antisolvent vapor-assisted crystallization method. Their phonon energies are comparatively studied by using Raman spectroscopy and temperature-dependent PL spectroscopy. More importantly, comparison studies of the multiphoton absorption (MPA) properties of $Cs_3Cu_2I_5$ and $CsCu_2I_3$ SCs are performed for the first time. Strong multiphoton excited PL emissions with large anisotropy factors are observed in these two types of SCs. Through the measurement of nonlinear transmittance, it is found that $CsCu_2I_3$ SCs exhibit much larger MPA coefficients compared with $Cs_3Cu_2I_5$ SCs, which is attributed to the larger density of states in the former. This work broadens the applications of cesium copper halides in nonlinear optoelectronics and light polarization related devices.

Introduction

All-inorganic cesium lead halide perovskites, including $CsPbX_3$ (X = Cl, Br, and I), have attracted considerable attention due to their extensive photonic and optoelectronic properties.[1,2] Given their high photoluminescence quantum yields (PLQYs), widely tunable bandgaps and high absorption coefficients, $CsPbX_3$ (X = Cl, Br, and I) materials have emerged as a class of semiconductors for high-performance optoelectronics, such as photovoltaics,[3,4] light-emitting diodes (LEDs),[5,6] photodetectors,[7] and lasers.[8] Moreover, these materials have been demonstrated to exhibit strong multiphoton absorption (MPA).[9] However, their inherent toxicity from the metal lead and poor material stability are also worthy of attention. Fortunately, all-inorganic low-dimensional cesium copper halides do not contain toxic lead ions and exhibit unique photophysical properties due to their stronger quantum confinement effect and higher stability, which make them promising substitutes for traditional $CsPbX_3$ (X = Cl, Br, and I) in various optoelectronic applications.[10–15]

Since Jun *et al.* first reported the synthesis of 0D $Cs_3Cu_2I_5$ single crystals (SCs) with a high PLQY of 90% and air stability,[16] low-dimensional cesium copper halides have emerged as novel optoelectronic materials due to their strong self-trapped excitons (STEs) and high PLQYs.[17] Subsequently, a lot of attention has been focused on the controllable synthetic strategies, structure characterization and linear optical properties of cesium copper halides, and on their applications in optoelectronics. For example, $Cs_3Cu_2I_5$ nanocrystals were used by Wang *et al.* to manufacture high-efficiency deep-blue LEDs with a half-lifetime above 100 h.[14] Fang's group successfully applied optically anisotropic 1D $CsCu_2I_3$ nanowires to manufacture polarization-sensitive and flexible UV photodetectors.[11] However, there is a lack of research on the nonlinear optical characteristics of cesium copper halides, including their MPA, which has several merits including a greater penetration depth,

[a] Key Laboratory of Optoelectronic Devices and Systems of Ministry of Education and Guangdong Province, College of Physics and Optoelectronic Engineering, Shenzhen University, Shenzhen 518060, China. E-mail: tche@szu.edu.cn
[b] Department of Electrical and Electronic Engineering, Southern University of Science and Technology, Shenzhen 518055, China. E-mail: chenr@sustech.edu.cn
[c] Key Laboratory of Green Preparation and Application for Functional Materials, Ministry of Education, School of Materials Science and Engineering, Hubei University, Wuhan 430062, China. E-mail: rkpan@hubu.edu.cn
[d] SZU-NUS Collaborative Innovation Center for Optoelectronic Science & Technology, International Collaborative Laboratory of 2D Materials for Optoelectronics Science and Technology of Ministry of Education, College of Physics and Optoelectronic Engineering, Shenzhen University, Shenzhen 518060, China

† Electronic supplementary information (ESI) available. See DOI: 10.1039/d0tc04061d

‡ These authors contributed equally to this work.

less damage to the samples, and higher spatial resolution.[18,19] The absence of relevant study hinders the further application of cesium copper halides in nonlinear photonic devices.

In this work, two types of cesium copper iodine SCs, *i.e.*, $CsCu_2I_3$ and $Cs_3Cu_2I_5$, were synthesized and their MPA properties were investigated. It was found that both $CsCu_2I_3$ and $Cs_3Cu_2I_5$ SCs exhibit efficient MPA. In addition, the yellow-emitting $CsCu_2I_3$ SCs show larger MPA coefficients than the blue-emitting $Cs_3Cu_2I_5$ SCs, while the latter exhibits higher multiphoton-excited PL anisotropy. Importantly, the MPA coefficients and anisotropy of these SCs can be greatly modified by adjusting the stoichiometric molar ratio of the precursors during the synthesis stage.

Experimental section

Materials

Cesium iodide (CsI, 99.9%), copper(I) iodide (CuI, 99.5%), dimethylformamide (DMF, 99.9%), dimethylsulfoxide (DMSO, 99.8%) and methanol (MeOH, AR) were purchased from Sigma Aldrich. All reagents and solvents were used without further purification.

Synthesis of SCs

$Cs_3Cu_2I_5$ SCs were grown using an antisolvent vapor-assisted crystallization method.[16] In detail, 3.897 g of CsI and 1.905 g of CuI were dissolved in 5 mL of DMSO and stirred at 60 °C until a clear solution was obtained. Then, methanol was dropwise added to the obtained solution until a precipitate appeared. The saturated solution was filtered using 0.45 μm PTFE filters and then poured into a vial, which was sealed using parafilm with small holes. This vial was placed inside a beaker filled with MeOH and sealed using parafilm. After growth at 60 °C for 24 hours, millimeter-sized high-quality $Cs_3Cu_2I_5$ SCs were obtained. The synthesis of $CsCu_2I_3$ SCs was similar to that of $Cs_3Cu_2I_5$ SCs, but it was adjusted by changing the molar ratio of CsI and CuI in the precursor solution. Specifically, 1.299 g of CsI and 0.952 g of CuI were dissolved in a mixed solvent of 1 mL of DMSO and 4 mL of DMF. The millimeter-sized high-quality $CsCu_2I_3$ SCs were finally obtained following the above method.

Sample characterization

XRD patterns were recorded using a MiniFlex600 X-ray diffractometer equipped with Cu Kα radiation. Excitation and emission spectra, absolute PLQYs and temperature-dependent PL spectra were collected using an Edinburgh FLSP920 spectrophotometer that is equipped with a calibrated integrating sphere and a cryogenic fluorescence system. Lifetime was recorded with the time-correlated single-photon counting technique using an Edinburgh FLS920 lifetime system, in which the excitation wavelength was set at 290 nm.

Measurements of two- and three-photon excited PL spectra

The fs pulses at the wavelengths of 600 and 800 nm, which were output from TOPAS (1000 Hz, 100 fs, Spectra-Physics, Inc.), were adopted as the excitation source. A series of neutral density filters was employed to control the incident energy of the laser pulses. The laser beam was focused onto the cesium copper iodide SCs *via* an Olympus BX43 fluorescence microscope. The spot sizes of the fs pulses on the SCs were ~4 μm at 600 nm and ~6 μm at 800 nm, respectively. During measurements, the multiphoton-excited PL signals can pass through a dichroic mirror, but the excitation light will be filtered by the dichroic mirror (Fig. S3, ESI†). After further filtration using an achromatic low-pass filter (<750 nm), the PL signals are then collected using a 20× objective lens with NA = 0.45 before reaching the spectrometer (SpectraPro HRS-300).

Determination of MPA coefficients

The MPA coefficients of $Cs_3Cu_2I_5$ and $CsCu_2I_3$ SCs were determined using our home-built micro-area nonlinear optical characterization system. During the measurements, broadband ultrafast variable attenuators (Newport VA-BB) were employed to control the incident energy of the laser pulses. A video microscope system (Olympus BX43) was constructed using a confocal microscope and an imaging development camera. The transmitted light passing through the cesium copper iodide crystals was first collected using a 20× objective lens with NA = 0.45 and was then detected using a silicon detector.

Results and discussion

Two types of millimeter-sized $CsCu_2I_3$ and $Cs_3Cu_2I_5$ SCs with high-crystallinity were successfully synthesized using an antisolvent vapor-assisted crystallization method, as shown in Fig. 1a and Fig. S1 (ESI†). By changing the molar ratio of cesium iodide (CsI) and copper(I) iodide (CuI) in the precursor solution, $Cs_3Cu_2I_5$ and $CsCu_2I_3$ SCs with different optical properties can be obtained. The crystal phase of these as-grown samples was confirmed using powder X-ray diffraction (XRD) analysis. The XRD patterns of $Cs_3Cu_2I_5$ and $CsCu_2I_3$ SCs coincide well with their standard XRD patterns, as depicted in Fig. 1b and c. As shown by the schematic crystal structure

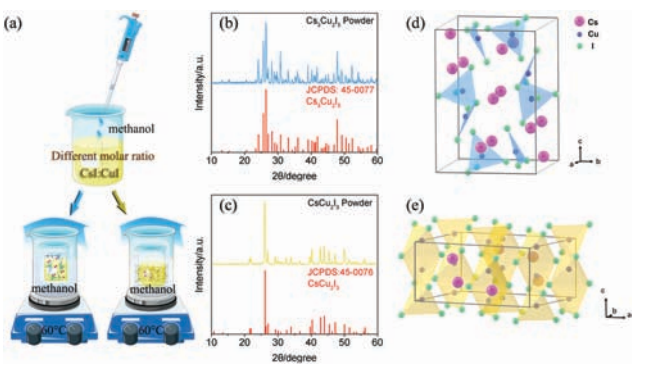

Fig. 1 (a) Schematic procedures for the synthesis of cesium copper iodide SCs. Powder XRD patterns of the as-prepared (b) $Cs_3Cu_2I_5$ and (c) $CsCu_2I_3$ SCs and the standard XRD patterns of these materials for comparison. Crystal structures of (d) $Cs_3Cu_2I_5$ and (e) $CsCu_2I_3$ SCs. Pink, purple, and green spheres represent Cs, Cu, and I, respectively.

(Fig. 1d), $Cs_3Cu_2I_5$ with a 0D electronic structure crystallizes in the orthorhombic space group of *Pnma* featuring Cu^+I_4 tetrahedra and a Cu^+I_3 triangle that are edge-connected to form isolated $[Cu_2I_5]^{3-}$ units separated by the surrounding Cs^+ ions.[20] In contrast, 1D $CsCu_2I_3$ crystallizes in the *CmCm* space group of the orthorhombic crystal system, in which Cu^+I_4 tetrahedra share common edges thereby forming infinite double chains of the composition of Cu_2I_3 interspersed by Cs^+ ions (Fig. 1e).

We first investigated the linear optical properties of these as-prepared SCs at 80 and 300 K. Fig. 2a and b display the emission and excitation spectra of $Cs_3Cu_2I_5$ and $CsCu_2I_3$ SCs, respectively. At 300 K, $Cs_3Cu_2I_5$ SCs exhibit a strong emission peak at 445 nm with a high PLQY up to 83% (Fig. S2, ESI†) and a large full-width at half-maximum (FWHM) of ~85 nm, which is well consistent with the previous literature.[16] The broad band PL emission with a large Stokes shift is the characteristic of STE emission for copper-based halides.[17] Compared with the emission spectrum at 80 K, the PL FWHM at 300 K broadens significantly, which indicates that more phonons and excitons are coupled at higher temperatures.[21] In 0D $Cs_3Cu_2I_5$, there is only one possible way to form a Cu–Cu bond for trapping excitons in a $[Cu_2I_5]^{3-}$ cluster,[22] which explains the absence of multiple STEs in 0D $Cs_3Cu_2I_5$ SCs. By contrast, for $CsCu_2I_3$ SCs at 300 K, there are two emitting peaks at 443 and 575 nm, corresponding to the radiative recombination of two different STEs. In addition, the latter exhibits a large FWHM of ~122 nm and a PLQY of 18%. Due to the 1D structure of the $CsCu_2I_3$ SCs, there are multiple Cu neighbors near each Cu atom, which allows the formation of Cu–Cu bonds in the excited state in different ways, resulting in multiple STEs.[22] Notably, for this kind of SC, the short-wavelength PL peak is suppressed at low temperature. Although previous literature explained the origin for this in terms of a reduction of temperature activation,[23] this needs to be further clarified with more evidence. The PL lifetimes of $Cs_3Cu_2I_5$ and $CsCu_2I_3$ SCs were also characterized. For the former, the PL decay curves at 80 and 300 K show no obvious change, and the single exponential fitting results show that their PL lifetimes probed at 445 nm are 1.21 and 1.48 μs, respectively (Fig. 2c). However, the PL lifetime of $CsCu_2I_3$ SCs probed at 575 nm is greatly prolonged from 0.42 μs at 300 K to 1.39 μs at 80 K (Fig. 2d), which is due to the thermally assisted de-trapping route and the temperature-dependent rapid non-radiative recombination.[24] Through the above process, the exciton–phonon coupling restores the twisted lattice around the STE to its original state. Therefore, higher temperatures accelerate de-trapping and facilitate relaxation *via* the rapid non-radiative process, which well explains the shortening of PL lifetime at higher temperatures.

Understanding the interaction between carrier and phonon is a prerequisite for manufacturing nonlinear photonic devices, and strong electron–phonon coupling is also crucial for the formation of STEs.[25] Although such characteristics of cesium copper iodides have been reported,[21,26,27] the related comparison study using Raman spectroscopy and a temperature-dependent PL spectroscopy method has not been reported yet. Fig. 3a and b show the temperature-dependent PL pseudo-color map of $Cs_3Cu_2I_5$ and $CsCu_2I_3$ SCs, respectively. With the increase of temperature, $CsCu_2I_3$ SCs exhibit a slight blue shift of the PL peak position, while no significant change for $Cs_3Cu_2I_5$ SCs is observed, indicating the better thermal color purity of the latter. Fig. 3c and d show the PL FWHM of $Cs_3Cu_2I_5$ and $CsCu_2I_3$ SCs as a function of temperature. The relevant values of the FWHM for $Cs_3Cu_2I_5$ SCs are larger compared with $CsCu_2I_3$ SCs, which can be attributed to the stronger electron–phonon coupling in 0D $Cs_3Cu_2I_5$ than in 1D $CsCu_2I_3$. The FWHM thermal broadening can be evaluated using the Huang–Rhys factor (S) and the phonon frequency ($\hbar\omega_{phonon}$), which can be described using the following equation:[28]

$$\mathrm{FWHM} = 2.36\sqrt{S}\hbar\omega_{\mathrm{phonon}}\sqrt{\coth\frac{\hbar\omega_{\mathrm{phonon}}}{2k_{\mathrm{B}}T}} \quad (1)$$

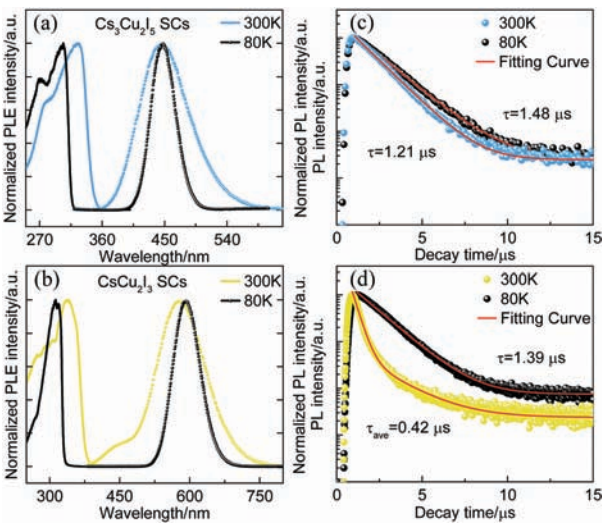

Fig. 2 Emission and excitation spectra of (a) $Cs_3Cu_2I_5$ and (b) $CsCu_2I_3$ SCs, measured at 80 and 300 K. Time-resolved PL decay and fitting curves of (c) $Cs_3Cu_2I_5$ and (d) $CsCu_2I_3$ SCs, measured at 80 and 300 K.

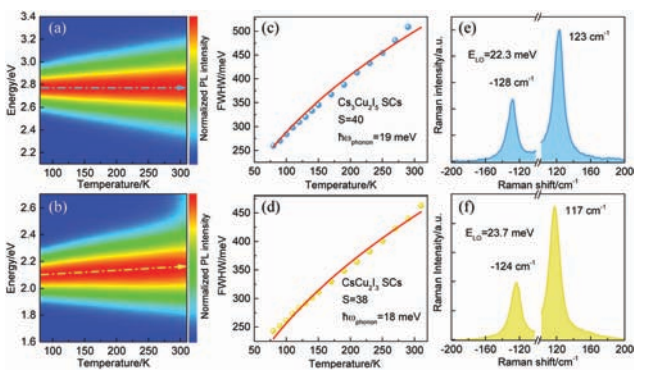

Fig. 3 Pseudocolor map of the temperature-dependent PL spectra of (a) $Cs_3Cu_2I_5$ and (b) $CsCu_2I_3$ SCs. The fitting results of the FWHM of (c) $Cs_3Cu_2I_5$ and (d) $CsCu_2I_3$ SCs as a function of temperature from 80 to 310 K. Raman spectra of (e) $Cs_3Cu_2I_5$ and (f) $CsCu_2I_3$ SCs. Stokes Raman spectra (left) and anti-Stokes Raman spectra (right) are shown in the figure.

The S factor and $\hbar\omega_{phonon}$ were calculated to be 40 and 19 meV for $Cs_3Cu_2I_5$ SCs, while the relevant values were determined as 38 and 18 meV for $CsCu_2I_3$ SCs, respectively. Such high S factors indicate a strong exciton–phonon coupling in the soft halide matrix, which promotes the formation of STEs.[21,25] Furthermore, we measured the Stokes and anti-Stokes Raman spectra of these as-grown SCs to determine their longitudinal optical (LO) phonon energies, as can be seen in Fig. 3e and f. The Stokes Raman spectra are dominated by the modes at 123 cm^{-1} ($Cs_3Cu_2I_5$) and 117 cm^{-1} ($CsCu_2I_3$), which are assigned to the vibration of I–Cu–I.[23] The anti-Stokes Raman peak indicates that the relaxation of excited electrons under resonance conditions will produce LO phonons.[29] The anti-Stokes Raman modes at −128 cm^{-1} ($Cs_3Cu_2I_5$) and −124 cm^{-1} ($CsCu_2I_3$) clearly exhibited their LO phonon modes. According to the previous literature,[29] the phonon energy ($\hbar\omega_{phonon}$) can be obtained from the Raman spectra according to the following equations:

$$\frac{I_{AS}}{I_S} \approx \frac{N_{LO}}{N_{LO}+1} \quad (2)$$

$$N_{LO} = \frac{1}{\left[\exp\left(\frac{\hbar\omega_{LO}}{K_B T}\right) - 1\right]} \quad (3)$$

where I_{AS} and I_S are the anti-Stokes and Stokes intensities in the Raman spectra, respectively. N_{LO} is the LO phonon occupation number. $\hbar$ is the Planck constant, ω_{LO} is the phonon frequency of the LO mode, K_B is the Boltzmann constant and T is the temperature in Kelvin. At 300 K, the phonon energies ($\hbar\omega_{LO}$) calculated for the LO phonon modes are 22.3 meV for $Cs_3Cu_2I_5$ and 23.7 meV for $CsCu_2I_3$.

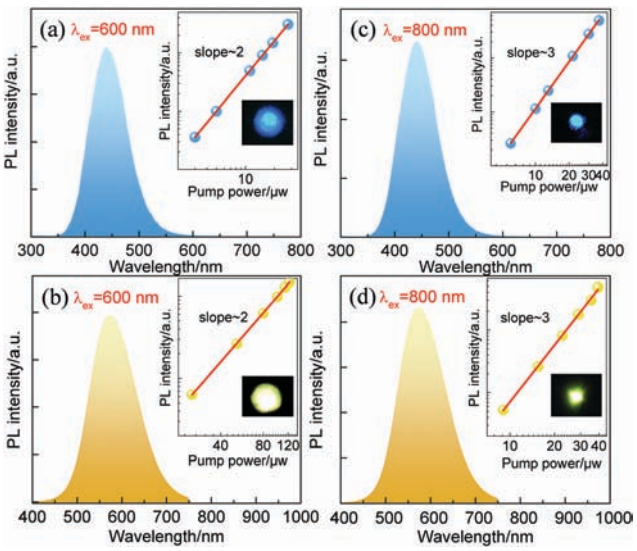

Fig. 4 Two-photon excited PL spectra of (a) $Cs_3Cu_2I_5$ and (b) $CsCu_2I_3$ excited by fs pulses at 600 nm. Three-photon excited PL spectra of (c) $Cs_3Cu_2I_5$ and (d) $CsCu_2I_3$ excited by fs pulses at 800 nm. Insets are plots of PL intensity *versus* optical intensity and emission images under multi-photon excitation.

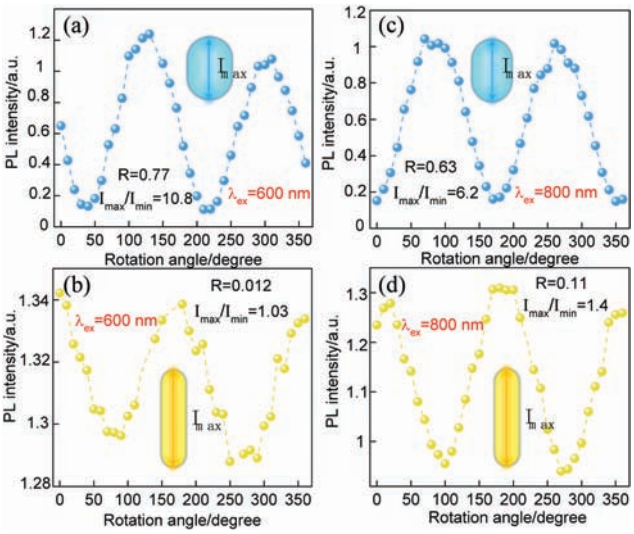

Fig. 5 Two-photon excited PL intensitiy of (a) $Cs_3Cu_2I_5$ and (b) $CsCu_2I_3$ SCs as a function of rotation angle of the analyzer plate. Three-photon excited PL intensity of (c) $Cs_3Cu_2I_5$ and (d) $CsCu_2I_3$ SCs as a function of rotation angle of the analyzer plate. Inset: I_{max} represents the emission intensity parallel to the excitation polarization direction.

According to the excitation spectra of cesium copper iodide SCs, it is expected that two- and three-photon absorption (2PA and 3PA) may be achieved under fs pulse excitation at the wavelengths of 600 and 800 nm, respectively. The multiphoton-excited PL spectra were then measured in order to confirm the occurrence of MPA processes. Whether excited at 600 or 800 nm, the PL spectra are indistinguishable from those in the case of one-photon excitation, indicating that the same emission states are involved in the cases of one-photon and multiphoton excitation (Fig. 4). From the analysis of the pumping fluence-dependent PL spectra (insets in Fig. 4a–d),

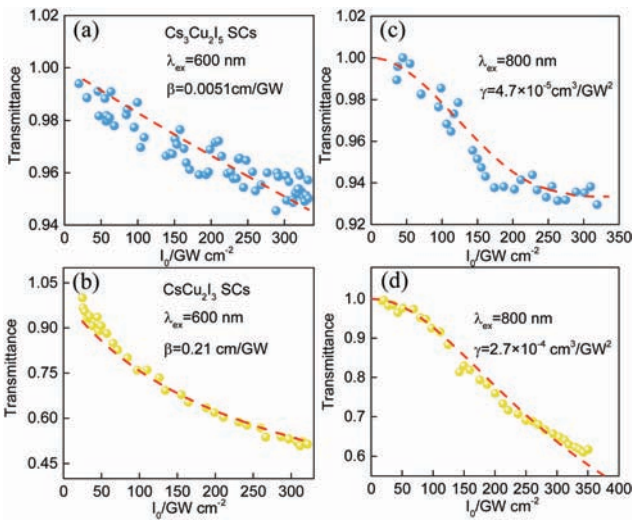

Fig. 6 The experimental data of nonlinear transmittance at different incident optical intensities and the corresponding theoretical fitted curves of (a) $Cs_3Cu_2I_5$ and (b) $CsCu_2I_3$ SCs excited using fs pulses at 600 nm and (c) $Cs_3Cu_2I_5$ and (d) $CsCu_2I_3$ SCs excited using fs pulses at 800 nm.

Table 1 Photophysical parameters of $Cs_3Cu_2I_5$ and $CsCu_2I_3$ SCs measured at 300 K

Materials	PL (nm)	τ_{ave} (μs)	$E_{LO}{}^a$ (meV)	$E_{LO}{}^b$ (meV)	R_{2PA}	2PA (cm GW^{-1})	R_{3PA}	3PA (cm^3 GW^{-2})
$Cs_3Cu_2I_5$	445	1.21	22.3	19	0.77	5.1×10^{-3}	0.63	4.7×10^{-5}
$CsCu_2I_3$	577	0.42	23.7	18	0.012	2.1×10^{-1}	0.11	2.7×10^{-4}

[a] Measured using Raman spectroscopy. [b] Measured using temperature-dependent PL spectroscopy.

the square and cubic relationships indicate that 2PA and 3PA occurred at 600 and 800 nm, respectively.

Anisotropic light-emitting materials tend to induce polarization of both the absorption and emission due to the unequal electric field strength along the asymmetric structure or grain dimensional difference.[30] Therefore, we further explored the MPA-induced PL emission anisotropy of $Cs_3Cu_2I_5$ and $CsCu_2I_3$ SCs, which was investigated by changing the rotation angle of the analyzer plate placed on the collection channel of the PL spectrometer. Generally, for an elongated structure, the emission along the long axis will be higher than the emission perpendicular to that axis when excited using linearly polarized light. Such a difference is called emission anisotropy and can be quantified by calculating the relevant I_{max}/I_{min} value, where I_{max} and I_{min} represent the emission intensity parallel and perpendicular to the excitation polarization direction, respectively. The multiphoton-excited PL emission anisotropy of the $Cs_3Cu_2I_5$ and $CsCu_2I_3$ SCs was then analyzed by rotating a polarizer (Fig. S3, ESI†). From the rotation angle dependent multiphoton-excited PL intensity shown in Fig. 5, the resulting values of I_{max}/I_{min} in $Cs_3Cu_2I_5$ SCs were calculated to be 10.8 (excited at 600 nm) and 6.2 (excited at 800 nm). For $CsCu_2I_3$ SCs, much smaller values of 1.03 (excited at 600 nm) and 1.4 (excited at 800 nm) were obtained. The anisotropy factor (R) is defined as $R = (I_{max} - I_{min})\ (I_{max} + 2I_{min})$.[31] It was found that when excited at either 600 or 800 nm, the anisotropy factors of the slender $CsCu_2I_3$ crystals are much smaller compared with $Cs_3Cu_2I_5$ SCs. This difference is caused by the difference in the internal structure asymmetry of the $Cs_3Cu_2I_5$ and $CsCu_2I_3$ SCs (Fig. S4, ESI†).[32]

Furthermore, the 2PA and 3PA coefficients of the $Cs_3Cu_2I_5$ and $CsCu_2I_3$ SCs were quantitatively determined using our home-built micro-area nonlinear optical characterization system (Fig. S5, ESI†). As shown in Fig. 6, the transmitted light intensity of the SCs decreases with an increase in the incident light intensity owing to the MPA mechanism. The 2PA coefficient (β) of the SCs can be obtained using the following equation:[33]

$$T(I_0) = \frac{I_t}{I_0} = \frac{[\ln(1 + I_0 l\beta)]}{I_0 l\beta} \quad (4)$$

where I_t is the transmitted light intensity, I_0 is the incident light intensity, and l is the thickness of the samples. By fitting the experimental data, the best-fitted β values of $Cs_3Cu_2I_5$ and $CsCu_2I_3$ SCs were determined to be $\sim 5.1 \times 10^{-3}$ and ~ 0.21 cm GW^{-1} (Fig. 6a and b), respectively. Notably, the 2PA coefficient of $CsCu_2I_3$ SCs is two orders of magnitude larger than that of $Cs_3Cu_2I_5$ SCs, which may be ascribed to the larger density of states in the former.[34,35] In addition, it was found that the 2PA coefficient of $CsCu_2I_3$ SCs is comparable to that of some lead-based perovskite materials, including $CH_3NH_3PbBr_3$ SCs (~ 5.2 cm GW^{-1} at 1000 nm),[36] but much larger compared with that of $C_6H_5CH_2NH_3PbBr_3$ thin film ($\sim 8.6 \times 10^{-3}$ cm GW^{-1} at 800 nm).[37] We proceeded to determine the 3PA coefficient (γ) of these SCs, and the corresponding experimental results are presented in Fig. 6c and d, which can be theoretically fitted using the following equation:[38]

$$T(I_0) = \frac{I_t}{I_0} = \frac{1}{\sqrt{1 + 2\gamma I_0^2 l}} \quad (5)$$

If the input light intensity is high enough, a 3PA saturation effect may be observed, and eqn (5) will become:[39]

$$T(I_0) = \frac{I_t}{I_0} = \frac{1}{\sqrt{1 + 2\gamma I_0^2 l \Big/ \left[1 + \left(\frac{I_0}{I_s}\right)^3\right]}} \quad (6)$$

where I_s is the saturation intensity. In our case, it was found that the experimental results for the $Cs_3Cu_2I_5$ SCs can be well fitted using eqn (6). However, the theoretical fitting using eqn (5) is more suitable for the $CsCu_2I_3$ SCs, due to the absence of the 3PA saturation effect. As a result, the γ values for $Cs_3Cu_2I_5$ and $CsCu_2I_3$ SCs can be extracted as 4.7×10^{-5} and 2.7×10^{-4} cm^3 GW^{-2}, respectively. In addition, the 3PA saturable light intensity of $Cs_3Cu_2I_5$ SCs is 337 GW cm^{-2}. It was found the 3PA coefficients of $CsCu_2I_3$ and $Cs_3Cu_2I_5$ SCs are much smaller than those of $CsPbBr_3$ SCs (1.4×10^{-1} cm^3 GW^{-2} at 1200 nm),[40] but comparable or larger than those of $CH_3NH_3PbBr_3$ microcrystals (2.26×10^{-5} cm^3 GW^{-2} at 1240 nm).[41] Again, the γ value of $CsCu_2I_3$ SCs was larger than that of the $Cs_3Cu_2I_5$ SCs. Although the MPA coefficients of $CsCu_2I_3$ and $Cs_3Cu_2I_5$ SCs are not extremely large, their high stability and non-toxic nature make them promising for various nonlinear photonic applications. In order to facilitate comparison, the photophysical parameters of $Cs_3Cu_2I_5$ and $CsCu_2I_3$ SCs are summarized in Table 1.

Conclusions

In summary, two types of all-inorganic lead-free cesium copper iodine ($CsCu_2I_5$ and $Cs_3Cu_2I_3$) SCs with high crystalline quality and PLQYs were successfully synthesized using an antisolvent vapor-assisted crystallization method, and their linear and nonlinear photophysical properties were investigated. Compared with $CsCu_2I_3$ SCs, $Cs_3Cu_2I_5$ SCs exhibit a larger multiphoton-excited PL anisotropy but much lower MPA coefficients. This work

suggests the promising applications of cesium copper iodine SCs in nonlinear optoelectronics and light polarization related devices.

Conflicts of interest

There are no conflicts to declare.

Acknowledgements

We acknowledge the financial support provided by the Natural Science Foundation of Guangdong Province (2019A15150-12094), the Project of Department of Education of Guangdong Province (2018KTSCX19) and the Shenzhen Basic Research Project of Science and Technology (JCYJ20190808121211510).

Notes and references

1 Y. Fu, H. Zhu, J. Chen, M. P. Hautzinger, X. Y. Zhu and S. Jin, *Nat. Rev. Mater.*, 2019, **4**, 169–188.
2 W. Xiang and W. Tress, *Adv. Mater.*, 2019, **31**, 1902851.
3 W. Xiang, Z. Wang, D. J. Kubicki, X. Wang, W. Tress, J. Luo, J. Zhang, A. Hofstetter, L. Zhang, L. Emsley, M. Grätzel and A. Hagfeldt, *Nat. Commun.*, 2019, **10**, 4686.
4 H. Zhang, X. Fu, Y. Tang, H. Wang, C. Zhang, W. W. Yu, X. Wang, Y. Zhang and M. Xiao, *Nat. Commun.*, 2019, **10**, 1088.
5 M. Lu, Y. Zhang, S. Wang, J. Guo, W. W. Yu and A. L. Rogach, *Adv. Funct. Mater.*, 2019, **29**, 1902008.
6 H. Wang, X. Zhang, Q. Wu, F. Cao, D. Yang, Y. Shang, Z. Ning, W. Zhang, W. Zheng, Y. Yan, S. V. Kershaw, L. Zhang, A. L. Rogach and X. Yang, *Nat. Commun.*, 2019, **10**, 665.
7 M. Gong, R. Sakidja, R. Goul, D. Ewing, M. Casper, A. Stramel, A. Elliot and J. Z. Wu, *ACS Nano*, 2019, **13**, 1772–1783.
8 X. Huang, Q. Guo, S. Kang, T. Ouyang, Q. Chen, X. Liu, Z. Xia, Z. Yang, Q. Zhang and J. Qiu, *ACS Nano*, 2020, **14**, 3150–3158.
9 Y. Wang, X. Li, X. Zhao, L. Xiao, H. Zeng and H. Sun, *Nano Lett.*, 2016, **16**, 448–453.
10 Y. Li, Z. Shi, W. Liang, L. Wang, S. Li, F. Zhang, Z. Ma, Y. Wang, Y. Tian, D. Wu, X. Li, Y. Zhang, C. Shan and X. Fang, *Mater. Horiz.*, 2020, **7**, 530–540.
11 Y. Li, Z. Shi, L. Wang, Y.-C. Chen, W. Liang, D. Wu, X. Li, Y. Zhang, C.-X. Shan and X. Fang, *Mater. Horiz.*, 2020, **7**, 1613–1622.
12 Z. Li, Z. Li, Z. Shi and X. Fang, *Adv. Funct. Mater.*, 2020, **30**, 2002634.
13 Z. Ma, Z. Shi, C. Qin, M. Cui, D. Yang, X. Wang, L. Wang, X. Ji, X. Chen, J. Sun, D. Wu, Y. Zhang, X. J. Li, L. Zhang and C. Shan, *ACS Nano*, 2020, **14**, 4475–4486.
14 L. Wang, Z. Shi, Z. Ma, D. Yang, F. Zhang, X. Ji, M. Wang, X. Chen, G. Na, S. Chen, D. Wu, Y. Zhang, X. Li, L. Zhang and C. Shan, *Nano Lett.*, 2020, **20**, 3568–3576.
15 F. Zeng, Y. Guo, W. Hu, Y. Tan, X. Zhang, J. Feng and X. Tang, *ACS Appl. Mater. Interfaces*, 2020, **12**, 23094–23101.
16 T. Jun, K. Sim, S. Iimura, M. Sasase, H. Kamioka, J. Kim and H. Hosono, *Adv. Mater.*, 2018, **30**, 1804547.
17 Z. Guo, J. Li, R. Pan, J. Cheng, R. Chen and T. He, *Nanoscale*, 2020, **12**, 15560–15576.
18 G. S. He, P. P. Markowicz, T.-C. Lin and P. N. Prasad, *Nature*, 2002, **415**, 767–770.
19 W. Chen, S. Bhaumik, S. A. Veldhuis, G. Xing, Q. Xu, M. Grätzel, S. Mhaisalkar, N. Mathews and T. C. Sum, *Nat. Commun.*, 2017, **8**, 15198.
20 S. Hull and P. Berastegui, *J. Solid State Chem.*, 2004, **177**, 3156–3173.
21 L. Lian, M. Zheng, W. Zhang, L. Yin, X. Du, P. Zhang, X. Zhang, J. Gao, D. Zhang, L. Gao, G. Niu, H. Song, R. Chen, X. Lan, J. Tang and J. Zhang, *Adv. Sci.*, 2020, **7**, 2000195.
22 M.-H. Du, *ACS Energy Lett.*, 2020, **5**, 464–469.
23 R. Lin, Q. Guo, Q. Zhu, Y. Zhu, W. Zheng and F. Huang, *Adv. Mater.*, 2019, **31**, 1905079.
24 S. Yakunin, B. M. Benin, Y. Shynkarenko, O. Nazarenko, M. I. Bodnarchuk, D. N. Dirin, C. Hofer, S. Cattaneo and M. V. Kovalenko, *Nat. Mater.*, 2019, **18**, 846–852.
25 S. Li, J. Luo, J. Liu and J. Tang, *J. Phys. Chem. Lett.*, 2019, **10**, 1999–2007.
26 R. Roccanova, A. Yangui, G. Seo, T. D. Creason, Y. Wu, D. Y. Kim, M.-H. Du and B. Saparov, *ACS Mater. Lett.*, 2019, **1**, 459–465.
27 L. Lian, M. Zheng, P. Zhang, Z. Zheng, K. Du, W. Lei, J. Gao, G. Niu, D. Zhang, T. Zhai, S. Jin, J. Tang, X. Zhang and J. Zhang, *Chem. Mater.*, 2020, **32**, 3462–3468.
28 W. Stadler, D. M. Hofmann, H. C. Alt, T. Muschik, B. K. Meyer, E. Weigel, G. Müller-Vogt, M. Salk, E. Rupp and K. W. Benz, *Phys. Rev. B: Condens. Matter Mater. Phys.*, 1995, **51**, 10619–10630.
29 X. B. Zhang, T. Taliercio, S. Kolliakos and P. Lefebvre, *J. Phys.: Condens. Matter*, 2001, **13**, 7053–7074.
30 S. Vezzoli, M. Manceau, G. Leménager, Q. Glorieux, E. Giacobino, L. Carbone, M. De Vittorio and A. Bramati, *ACS Nano*, 2015, **9**, 7992–8003.
31 Y. Li, H. Huang, Y. Xiong, A. F. Richter, S. V. Kershaw, J. Feldmann and A. L. Rogach, *ACS Nano*, 2019, **13**, 8237–8245.
32 B. Siebers, L. Biadala, D. Yakovlev, A. Rodina, T. Aubert, Z. Hens and M. Bayer, *Phys. Rev. B: Condens. Matter Mater. Phys.*, 2015, **91**, 155304.
33 G. S. He, G. C. Xu, P. N. Prasad, B. A. Reinhardt, J. C. Bhatt and A. G. Dillard, *Opt. Lett.*, 1995, **20**, 435–437.
34 P. Cheng, L. Sun, L. Feng, S. Yang, Y. Yang, D. Zheng, Y. Zhao, Y. Sang, R. Zhang, D. Wei, W. Deng and K. Han, *Angew. Chem., Int. Ed.*, 2019, **58**, 16087–16091.
35 T. He, J. Li, X. Qiu, S. Xiao, C. Yin and X. Lin, *Adv. Opt. Mater.*, 2018, **6**, 1800843.
36 C. Kriso, M. Stein, T. Haeger, N. Pourdavoud, M. Gerhard, A. Rahimi-Iman, T. Riedl and M. Koch, *Opt. Lett.*, 2020, **45**, 2431–2434.
37 A. Mushtaq, D. Kushavah, S. Ghosh and S. K. Pal, *Appl. Phys. Lett.*, 2019, **114**, 051902.

38 G. S. He, J. D. Bhawalkar, P. N. Prasad and B. A. Reinhardt, *Opt. Lett.*, 1995, **20**, 1524–1526.
39 G. S. He, Q. Zheng, A. Baev and P. N. Prasad, *J. Appl. Phys.*, 2007, **101**, 083108.
40 D. Clark, C. Stoumpos, F. Saouma, M. G. Kanatzidis and J. Jang, *Phys. Rev. B*, 2016, **93**, 195202.
41 Y. Gao, S. Wang, C. Huang, N. Yi, K. Wang, S. Xiao and Q. Song, *Sci. Rep.*, 2017, **7**, 45391.